The importance of sulfur for the behavior of highly-siderophile elements during Earth's differentiation

Vera Laurenz *, David C. Rubie, Daniel J. Frost, Antje K. Vogel

Bayerisches Geoinstitut, Universität Bayreuth, 95440 Bayreuth, Germany

Abstract

The highly siderophile elements (HSEs) are widely used as geochemical tracers for Earth's accretion and core formation history. It is generally considered that core formation strongly depleted the Earth's mantle in HSEs, which were subsequently replenished by a chondritic late veneer. However, open questions remain regarding the origin of suprachondritic Ru/Ir and Pd/Ir ratios that are thought to be characteristic for the primitive upper mantle. In most core-formation models that address the behavior of the HSEs, light elements such as S entering the core have not been taken into account and high P–T experimental data for S-bearing compositions are scarce. Here we present a comprehensive experimental study to investigate the effect of increasing S concentration in the metal on HSE metal–silicate partitioning at 2473 K and 11 GPa. We show that the HSEs become less siderophile with increasing S concentrations in the metal, rendering core-forming metal less efficient in removing the HSEs from the mantle if S is present. Furthermore, we investigated the FeS sulfide–silicate partitioning of the HSEs as a function of pressure (7–21 GPa) and temperature (2373–2673 K). The sulfide–silicate partition coefficient for Pt increases strongly with P, whereas those for Pd, Ru and Ir all decrease. The combined effect is such that above ∼20 GPa Ru becomes less chalcophile than Pt, which is opposite to their behavior in the metal–silicate system where Ru is always more siderophile than Pt. The newly determined experimental results are used in a simple 2-stage core formation model that takes into account the effect of S on the behavior of the HSEs during core formation. Results of this model show that segregation of a sulfide liquid to the core from a mantle with substantial HSE concentrations plays a key role in reproducing Earth's mantle HSE abundances. As Ru and Pd are less chalcophile than Pt and Ir at high P–T, some Ru and Pd remain in the mantle after sulfide segregation. Addition of the late veneer then raised the concentrations of all HSE to their current levels. Suprachondritic Ru/Ir and Pd/Ir ratios of the mantle can thus be explained by a combination of sulfide segregation together with the addition of a late veneer without the need to invoke unknown chondritic material.
© 2016 The Authors. Published by Elsevier Ltd. This is an open access article under the CC BY-NC-ND license (http://creativecommons.org/licenses/by-nc-nd/4.0/).

Keywords: HSE; Core formation; Sulfide–silicate partitioning; Metal–silicate partitioning

1. INTRODUCTION

The defining property of the highly siderophile elements (HSEs – Re, Os, Ir, Ru, Pt, Pd, Rh, Au) is their strong affinity to partition into Fe-rich metal. Therefore, the HSEs are useful geochemical tracers of processes involving metal–silicate equilibration such as the formation of the Earth's

core (e.g. Kimura et al., 1974; Wänke, 1981; O'Neill, 1991; Righter et al., 2008; Walker, 2009). It is known from 1-bar solubility experiments (e.g. O'Neill et al., 1995; Borisov and Palme, 2000; Fortenfant et al., 2003, 2006; Ertel et al., 2008) as well as high P–T metal–silicate partitioning experiments (e.g. Holzheid et al., 2000; Righter et al., 2008; Brenan and McDonough, 2009; Mann et al., 2012) that segregation of metal to the Earth's core should have left the mantle much more depleted in HSEs than what is observed for the primitive upper mantle (PUM),

* Corresponding author.
E-mail address: vera.laurenz@uni-bayreuth.de (V. Laurenz).

which is generally used as a proxy for the whole mantle. Most experimental data also suggest a strong fractionation among the HSEs during metal–silicate equilibration (O'Neill et al., 1995; Brenan and McDonough, 2009; Mann et al., 2012), which is also not seen. Instead, the HSEs are thought to be present in roughly chondritic proportions in the PUM (e.g. Becker et al., 2006; Barnes et al., 2015). The most accepted model to explain the apparent overabundance and chondritic ratios of the HSEs is the so-called "late veneer" concept (e.g. Kimura et al., 1974; Wänke, 1981). After core formation ceased chondritic material was accreted to the Earth's mantle, thereby establishing the absolute and relative mantle HSE abundances. Such late accretion of chondritic material has proven to be a common feature of planetary bodies in the solar system (e.g. Day et al., 2007; Walker, 2009; Dale et al., 2012). Estimates of the amount of material added to Earth's mantle range from 0.3% to 1% of the total mass of the Earth (Morgan et al., 2001; Walker, 2009; Jacobson et al., 2014; Walker et al., 2015). A caveat of this theory is that in detail PUM appears to have suprachondritic Ru/Ir and Pd/Ir ratios, which cannot be reproduced by the late accretion of any known meteorite group (e.g. Becker et al., 2006; Walker, 2009). Lunar impact melt rocks appear to display similar suprachondritic Ru/Ir and Pd/Ir ratios. Therefore, it has been suggested that the late veneer could be composed of material that is either not represented by known meteorites (Wang and Becker, 2013; Fischer-Gödde et al., 2015; Walker et al., 2015), or consists of a mixture of CI-chondrite and iron-meteorite-like material (e.g. Fischer-Gödde and Becker, 2012; Kruijer et al., 2015).

Another possibility to explain suprachondritic Pd/Ir and Ru/Ir might be if some Pd and Ru were retained in the mantle during core-formation. While this is possible for the least siderophile element Pd, this cannot explain Ru/Ir, however, because Ru is too strongly siderophile at high P–T (at 30 GPa, 2673 K and FMQ-2 $D_{Pd} = 1.9 \times 10^3$, $D_{Ru} = 5.1 \times 10^5$ and $D_{Ir} = 2.4 \times 10^6$ – Mann et al., 2012). A potential solution could be the presence of light elements in core-forming metallic liquids. It has become increasingly apparent that light elements such as O, Si, C and S entering the core will affect the partitioning behavior of a range of trace elements (e.g. Jana and Walker, 1997a,b; Chabot and Agee, 2003; Wood et al., 2013; Righter et al., 2014; Fischer et al., 2015; Wang et al., 2016). For the behavior of the HSEs sulfur potentially plays an important role, as the HSEs are also strongly chalcophile elements (Peach et al., 1990; Fleet et al., 1991; Bezmen et al., 1994; Crocket et al., 1997; Pruseth and Palme, 2004; Fonseca et al., 2009, 2011, 2012; Mungall and Brenan, 2014). Sulfur can have an effect in two different ways: Firstly, the presence of S may influence the metal–silicate partitioning behavior of trace elements (e.g. Jana and Walker, 1997a; Cottrell et al., 2009; Mann et al., 2009; Rose-Weston et al., 2009; Righter, 2011; Wade et al., 2012; Wood et al., 2014). This may also be true for the HSEs because S^{2-} dissolved in silicate melts bonds with HSEs and thereby enhances their solubility (Laurenz et al., 2013; Mungall and Brenan, 2014), causing metal–silicate partition coefficients to decrease. Moreover, S present in the metal phase also

affects HSE partitioning. Partition coefficients for Pd reported by Righter et al. (2008) with up to 5 wt.% S in the metal phase are significantly lower than the results of Mann et al. (2012) for S-free metal. This indicates that S-bearing metals are potentially less efficient in extracting HSEs to the core.

Secondly, an immiscible sulfide melt may have exsolved from the magma ocean and segregated to the core (e.g. O'Neill, 1991; Wood and Halliday, 2005; Lee et al., 2007). This hypothesis was shown to be consistent with chalcophile element patterns of the mantle (e.g. Kiseeva and Wood, 2015) as well as its Cu-isotope signature (Savage et al., 2015). Sulfide–silicate partition coefficients of the HSEs at low P–T conditions are generally high and range between 10^3 and 10^8 (e.g. Fleet et al., 1991; Bezmen et al., 1994; Fonseca et al., 2009, 2012; Mungall and Brenan, 2014). Most recent determinations at 1 bar, 1473 K and ~FMQ-1 yield $D^{sulfide–silicate}$ between 4×10^5 for Ru and 3×10^6 for Pt and Ir (Mungall and Brenan, 2014). Although these data were generated at P–T conditions much lower than those inferred for the formation of Earth's core, they imply that HSEs could be efficiently extracted to the core by core-forming sulfide liquids (O'Neill, 1991).

The aim of this study is to assess the effect of S, either dissolved in metal or as immiscible sulfide melt, on the behavior of the HSEs during core formation. Therefore, we have investigated experimentally the effect of S on the metal–silicate partitioning behavior of the HSEs as well as their sulfide–silicate partitioning at high P–T conditions. From these experiments, we also determined the solubility of S in peridotite melts to ascertain under which conditions an immiscible sulfide melt can exsolve from a magma ocean. The results are applied to model the behavior of the HSEs during core formation, and to address the question of how the HSE abundances of the Earth's mantle were established.

2. EXPERIMENTAL PROCEDURES AND RUN PRODUCTS

Two sets of experiments were carried out to study the partitioning behavior of Pt, Pd, Ru and Ir at high temperatures and pressures. These HSEs were chosen in order to investigate the origin of possible suprachondritic Pd/Ir and Ru/Ir ratios in the Earth's mantle while maintaining a chondritic Pt/Ir ratio. These elements also include the most siderophile (Ir) as well as the least siderophile (Pd) of the HSEs. In the first set (Set 1) we equilibrated molten peridotite with a range of metal or sulfide compositions along the Fe–FeS binary join at constant P (11 GPa) and T (2473 K), to systematically study the effect of S on HSE metal–silicate partitioning. In the second set of experiments (Set 2) the sulfide–silicate partitioning of the HSEs was investigated by equilibrating FeS sulfide melt with molten peridotite at pressures from 7 to 21 GPa and temperatures between 2373 and 2673 K.

In both cases, the starting silicate composition was a synthetic peridotite corresponding to the primitive mantle composition (Palme and O'Neill, 2014). The peridotite composition was prepared from reagent-grade oxides and

carbonates, and was thoroughly mixed under ethanol. The silicate powder was decarbonized in air (1273 K) and subsequently reduced for 24 h in a 1-atm gas mixing furnace at 1473 K and an oxygen fugacity (fO$_2$) of FMQ-2 (2 log-units below the Fayalite-Magnetite-Quartz buffer – O'Neill and Wall, 1987). This is important because the HSEs show a tendency to form nano-nuggets in the silicate melt, which are a problem for later LA-ICP-MS analysis of the run products (e.g. Ertel et al., 2008; Laurenz et al., 2010, 2013). These nano-nuggets are thought to be formed at the beginning of an experiment as the result of an initially higher fO$_2$ compared to equilibrium run conditions (Ertel et al., 2006; Médard et al., 2015). Therefore, using a reduced silicate starting composition minimizes the formation of such nano-nuggets in the silicate liquid (Médard et al., 2015).

The starting metal compositions (Set 1) were mixed from pure Fe and FeS powders, while the starting sulfide (Set 2) consisted of only FeS. Only two HSEs were added to individual batches of these compositions as metal powders in the wt.% concentration levels (usually ~10–15 wt.% each), in order to maintain Fe-rich metal compositions. We performed experiments with different combinations of HSEs (Pt + Pd, Pt + Ru, Pd + Ir and pure Pd) and also varied Pd concentrations (~10 wt.% in Pt + Pd experiments and ~1 wt.% in Pd + Ir and pure Pd experiments) in order to test whether the partition coefficients vary with the identity of the other element and also as a function of Pd concentration.

In order to minimize the risk of incomplete metal/sulfide – silicate separation during the partitioning experiments, each metal or sulfide composition was fused for 20 min in a piston-cylinder apparatus at 1473 K and 1.5 GPa using MgO capsules, and subsequently cut into chips using a diamond wire saw (c.f. Mann et al., 2012). We first loaded a layer of peridotite powder into the MgO capsule, followed by metal/sulfide chips and then a second layer of silicate powder at the top so that the metal/sulfide chips were sandwiched between peridotite powder. Initially experiments were performed using polycrystalline MgO capsules. However, these were found to react strongly with the molten silicate during the experiment, so that single crystal MgO capsules were used in all subsequent experiments.

Partitioning experiments were carried out in a multianvil apparatus using MgO octahedra (doped with Cr$_2$O$_3$ to enhance thermal insulation) as the pressure medium. The edge length of the octahedra was 18 mm in all experiments, and two capsules could be run simultaneously end to end. Tungsten carbide cubes with 11 mm truncations (18/11 configuration) were used for experiments between 7 and 11 GPa in 1000 t and 5000 t Kawai-type presses. Experiments at 21 GPa were performed using an 18/8 configuration in the 5000 t Kawai-type press (Frost et al., 2004). Stepped LaCrO$_3$-heaters were used for all experiments in order to minimize the temperature gradient across the sample (Rubie, 1999). Temperatures of the experiments were monitored using W$_{97}$Re$_3$-W$_{75}$Re$_{25}$ (type D) thermocouples. Based on the variation of the temperature-power relationship, temperature uncertainties are estimated to be ±100 K. After a run time of 5 min the samples were

quenched rapidly (~250 K/s initially) by switching off the power and then slowly decompressed. The run time chosen for our experiments was guided by previous studies at similar P–T conditions. We expect equilibration between metal and silicate to be fast, given the high temperatures of our experiments (e.g. Thibault and Walter, 1995; Li and Agee, 2001). Corgne et al. (2008) and Mann et al. (2009) performed time-series experiments at high P and T (2273 K and 3.6 GPa as well as 2373 K and 6 GPa, respectively). Their results show that run durations of 120 s (or less) are sufficient to reach equilibrium, as partition coefficients for a range of elements were found to be constant with further increases in run time. On the other hand, the run duration has to be limited in order to avoid or minimize reaction of the silicate melt with the MgO capsule, which would result in numerous MgO-rich crystals dispersed throughout the melt. Therefore, we limited the run time of our experiments to ~5 min so that interaction of the silicate melt with the MgO capsule was minimized as is evident from the textures and chemical composition of the samples (c.f. Mann et al., 2009). A few initial experiments were run for only 2–3 min resulting in somewhat larger uncertainties in the HSE concentrations of the quenched silicate melt.

Typical run products consist of a sphere of quenched metal or sulfide surrounded by quenched silicate melt (Fig. 1). Metal and sulfide phases usually display fine-grained quench textures. Furthermore, an O-rich phase (oxides or silicates) exsolved in the central region of the spheres, whereas the rims are often devoid of this phase. Similar features have been observed previously, and were explained by exsolution of oxygen and its diffusion into the surrounding silicate during quenching (Geßmann and Rubie, 1998; O'Neill et al., 1998). The silicate contains elongate, skeletal olivine crystals that formed upon quenching. Interstitial pockets contain fine grained metal or sulfide phases along olivine grain boundaries, and are interpreted to be quench products (i.e. such products were dissolved in the molten silicate at run conditions – Mann et al., 2012).

3. ANALYTICAL METHODS

3.1. Electron microprobe

Experimental run products (metal, sulfide, quenched silicate and ferropericlase) were analyzed for their major element compositions with a JEOL JXA 8200 electron probe micro analyzer (EPMA) in wavelength dispersive mode (WDS). The results are listed in Tables EA1–EA3 in the electronic supplement. All quoted uncertainties are 1σ standard deviations.

Metals and sulfides were both analyzed with a 20 kV accelerating voltage and a 20 nA probe current. Pure metals were used as standards for Fe, Pt, Pd, Ru, Ir and Cr, while S, Si and O were calibrated on FeS$_2$, andradite and MgO, respectively. Matrix corrections were performed using the ZAF correction method. Because the Ru L$_\beta$-line interferes with the Pd L$_\alpha$-line, Pd was measured on the L$_\beta$-line. Peak counting times were 20 s for Fe, Pt, Ru, Ir and S, 60 s for Pd (due to the lower intensity of the Pd L$_\beta$-line) and 150 s for Si, O and Cr. Due to the quench textures in the metals
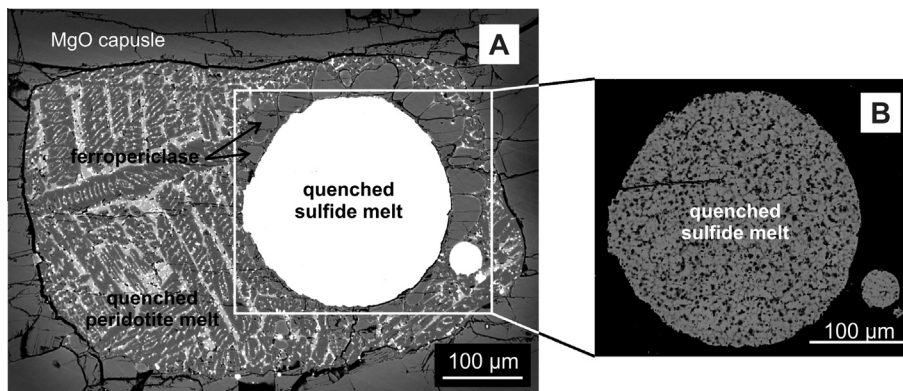
Fig. 1. Back scattered electron images of a typical experimental run product obtained at 11 GPa and 2473 K. (A) Overview of the entire sample. The single-crystal MgO-capsule contains a sulfide sphere in contact with quenched peridotite melt. The peridotite melt displays typical quench features including elongate olivine-crystals. Some ferropericlase crystallized close to the metal sphere and near the capsule walls. (B) The sulfide sphere showing the characteristic quench texture of crystalline sulfide (light gray), interstitial oxygen-rich sulfide (dark gray) and oxides (black).

and sulfides the variation among individual analyses can be high. Thus, calculating standard deviations from individual point-analyses would overestimate the uncertainty on the determined bulk composition. In order to average the composition of the quench phases, the electron beam was defocussed to 30 μm. In addition, analyses were performed along square grids with an edge length of 60 μm (3×3 points per grid) and the average was calculated for each grid. The reported standard deviation (1σ) is the uncertainty calculated among these averages for the individual grids. Averaging a number of microprobe measurements of similarly textured quenched metallic melts has previously been shown to yield accurate results compared to determining bulk concentrations by image analysis (Chabot and Drake, 1997).

Quenched silicate liquid and ferropericlase were both analyzed using a 15 kV accelerating voltage and 15 nA probe current. Standards used were natural silicates and oxides and pure metal for Cr. Matrix corrections were performed with the $-\phi(\rho z)$ correction method. The silicates were analyzed along grids with the beam defocussed to 30 μm, and reported average and standard deviation (1σ) values were calculated as described above. Peak counting times for the silicate analyses were 20 s for Si, Mg, Al, Ca and Fe and 100 s for Mn, Cr and Ti. The ferropericlases were analyzed in spot mode and peak counting times of 20 s for Mg and Ca, 60 s for Fe, Al and Si, and 180 s for Mn, Cr and Ti.

3.2. Laser ablation mass spectrometry

The concentrations of Pt, Pd, Ru and Ir in the quenched silicate melts were analyzed by laser ablation – inductively coupled plasma – mass spectrometry (LA-ICP-MS) using a Coherent COMPexPRO 102 excimer laser (193 nm) attached to a Perkin Elmer ELAN DRC-e quadrupole ICP-MS. The laser system was operated at a pulse rate of 5 Hz and an energy of 80 mJ. Spot size was 70–80 μm. The ablation chamber was flushed with He as the carrier

gas. Additional H_2 was admixed on the way to the mass spectrometer to enhance the sensitivity. Data were collected in time-resolved mode with ∼40 s of background measurement and ∼60 s of measurement with the laser turned on. Isotopes recorded were [23]Na, [25]Mg, [27]Al, [29]Si, [32]S, [34]S, [42]Ca, [49]Ti, [53]Cr, [55]Mn, [57]Fe, [101]Ru, [102]Ru, [105]Pd, [108]Pd, [139]La, [184]W, [185]Re, [191]Ir, [193]Ir, [194]Pt, [195]Pt. Chromium, La, W and Re were monitored in order to exclude possible contamination of the samples by the W-Re thermocouple and the $LaCrO_3$ heater. Using [29]Si as the internal standard, the HSE concentrations were quantified against the synthetic HSE-II glass reference material calibrated by Mann et al. (2012). The matrix of this glass has a eutectic anorthite-diopside composition and contains between 1 and 90 μg/g (ppm) Ru, Rh, Pd, Re, Ir and Pt as calibrated by solution ICP-MS.

In rare cases the spectra showed spikes in the HSE signals, which were attributed to the presence of metallic inclusions in the silicate. These inclusions are interpreted to represent stable phases also at run conditions and therefore do not represent HSE partitioning into silicate melts (Médard et al., 2015). In contrast, the finely dispersed quench phase along olivine grain boundaries (cf. Section 2) are homogeneously distributed in the sample and are not visible in the laser-spectra. Therefore, only ablation intervals between the spikes were quantified, following the approach of Ertel et al. (2006, 2008). If metal inclusions were incorporated in the calculation, equilibrium HSE concentrations in the silicate would be significantly overestimated because the inclusions are stable phases at run conditions.
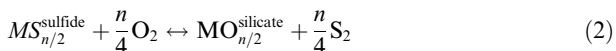
In order to calculate S concentrations in the silicate we used a basaltic silicate glass containing 5240 ppm S (SB19 from Botcharnikov et al., 2010) as a reference material. We employed [34]S instead of the more abundant [32]S, due to an interference of $^{16}O_2^+$ on $^{32}S^+$. NIST SRM 610 was run as an unknown throughout the course of this study, and calculated concentrations for Pd (1.38 ± 0.17 ppm), Pt (3.30 ± 0.25 ppm) and S (575 ± 79 ppm) agree with values

reported in the literature within the uncertainties (Pd: 1.21 ± 0.44 ppm; Pt: 3.12 ± 0.08 ppm; S: 575 ± 32 ppm – Sylvester and Eggins, 1997; Jochum et al., 2011).

4. RESULTS

4.1. Calculation of HSE exchange coefficients

The partitioning of a trace siderophile element M between metal and silicate melt or FeS sulfide melt and silicate melt is controlled by the following equilibria:

$$M^{\text{metal}} + \frac{n}{4}O_2 \leftrightarrow MO_{n/2}^{\text{silicate}} \tag{1}$$

$$MS_{n/2}^{\text{sulfide}} + \frac{n}{4}O_2 \leftrightarrow MO_{n/2}^{\text{silicate}} + \frac{n}{4}S_2 \tag{2}$$

where n is the valence state of the element M in the silicate melt. The molar partition coefficient D between metal and silicate melt is defined as:
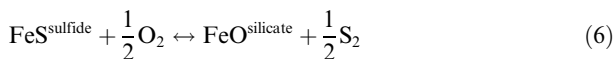
$$D_M^{\text{metal}-\text{silicate}} = \frac{X_M^{\text{metal}}}{X_M^{\text{silicate}}} \tag{3}$$

where X_M is the mole fraction of the element M in the metal or silicate respectively. The sulfide–silicate partition coefficient $D_M^{\text{sulfide}-\text{silicate}}$ can be expressed accordingly (with $X_{M_i}^{\text{sulfide}} = \frac{M_i}{\sum_{i=1}^{n} M_i}$). Additionally, Fe and the HSEs do not only dissolve as oxide species in silicate melts, but also as sulfide species (Klimm and Botcharnikov, 2010; Laurenz et al., 2013; Mungall and Brenan, 2014) according to:

$$MO_{n/2}^{\text{silicate}} + \frac{n}{4}S_2 \leftrightarrow MS_{n/2}^{\text{silicate}} + \frac{n}{4}O_2 \tag{4}$$
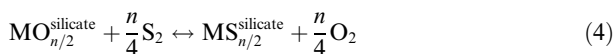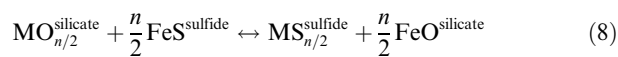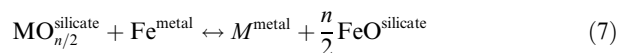
Measured concentrations of the HSEs in our experimental silicate melts used to calculate partition coefficients therefore represent the sum of HSE-oxide and HSE-sulfide species dissolved in the silicate melts.

Metal–silicate partition coefficients in S-free systems depend on fO_2 (Eq. (1)), whereas sulfur fugacity (fS_2) has to be taken into account as well, if an FeS–sulfide melt is present. Both fO_2 and fS_2 are governed by the partitioning of Fe according to the following equilibria:

$$Fe^{\text{metal}} + \frac{1}{2}O_2 \leftrightarrow FeO^{\text{silicate}} \tag{5}$$

$$FeS^{\text{sulfide}} + \frac{1}{2}O_2 \leftrightarrow FeO^{\text{silicate}} + \frac{1}{2}S_2 \tag{6}$$

We estimated fO_2 using the partitioning of Fe between metal or sulfide and ferropericlase (c.f. Mann et al., 2009). As the compositions in our study range from Fe-HSE alloys to HSE-FeS sulfides, we included an activity coefficient for Fe (γ_{Fe}) determined via an asymmetric multi-component Margules-type regular solution model (Mukhopadhyay et al., 1993, see Appendix for details). The estimated fO_2 of our experiments ranges from IW-1.5 to IW-0.5 (1.5 to 0.5 log units below the iron-wüstite buffer – O'Neill and Pownceby, 1993).

By combining Eqs. (1) and (5) as well as Eqs. (2) and (6), the exchange of a trace element M and Fe between coexisting metal or sulfide and silicate melt can be described through the following exchange reactions:

$$MO_{n/2}^{\text{silicate}} + Fe^{\text{metal}} \leftrightarrow M^{\text{metal}} + \frac{n}{2}FeO^{\text{silicate}} \tag{7}$$

$$MO_{n/2}^{\text{silicate}} + \frac{n}{2}FeS^{\text{sulfide}} \leftrightarrow MS_{n/2}^{\text{sulfide}} + \frac{n}{2}FeO^{\text{silicate}} \tag{8}$$

Metal–silicate and sulfide–silicate exchange coefficients can therefore be described relative to the partitioning of Fe:

$$K_D(M) = \frac{D_M}{(D_{\text{Fe}})^{n/2}} \tag{9}$$

In order to calculate $K_D(\text{metal} - \text{silicate})$ and $K_D(\text{sulfide} - \text{silicate})$ we assumed the HSEs to have the same valence state as determined for S-free experiments by Mann et al. (2012). Using exchange coefficients with Fe renders assumptions about fO_2 and fS_2 unnecessary, because fO_2 and fS_2 are determined through the partitioning of Fe according to Eq. (5). A similar approach was employed by Kiseeva and Wood (2013) and Brenan (2015) for sulfide–silicate partitioning of a range of elements. Since the composition of the sulfide melt does not change in their experiments, they directly express $D_M^{\text{sulfide}-\text{silicate}}$ as a function of the FeO concentration of their silicate melts. Partition coefficients and exchange coefficients for the HSEs calculated from our experiments ($D^{\text{exp}}(\text{HSE})$ and $K_D^{\text{exp}}(\text{HSE})$ respectively) are summarized in the Supplementary Tables EA 4 and EA 5.

To facilitate analysis of HSE concentrations by LA-ICP-MS in the quenched peridotite melt we have added the HSEs in wt.% concentration levels (between 1 wt.% and 15 wt.% each – see Section 2) to the metals and sulfides of our experiments. Thus, activity coefficients of the HSEs may no longer obey Henry's law, but depend on the concentrations of the elements in the metal or sulfide. Therefore, we corrected experimentally-determined exchange coefficients ($K_D^{\text{exp}}(\text{HSE})$) to infinite dilution ($K_D^0(\text{HSE})$) in order to be able to apply our results to the segregation of the Earth's core (c.f. Mann et al., 2012). This procedure takes into account the activity coefficients of Fe and the HSEs (γ_{Fe}, γ_{HSE}) in the experimentally-produced metal and sulfide compositions as well as activity coefficients of the HSEs corresponding to the concentration level at infinite dilution (γ_{HSE}^0):

$$K_D^0(\text{HSE}) = K_D^{\text{exp}}(\text{HSE}) \times \frac{\gamma_{\text{HSE}}}{\gamma_{\text{HSE}}^0 * (\gamma_{\text{Fe}})^{n/2}} \tag{10}$$

Activity coefficients were derived using an asymmetric multicomponent Margules-type regular solution model (Mukhopadhyay et al., 1993). We employed binary Margules interaction parameters for the Fe-HSE and HSE-HSE systems which were compiled by Mann et al. (2012) from the literature. For Fe–S we used the activity–composition relations presented by Nagamori et al. (1970) while interaction parameters for HSE-S were fitted to solid metal–liquid metal partitioning data as a function of S (Chabot and Drake, 1997; Chabot and Jones, 2003; Chabot et al., 2003, 2007, 2009). Details of our correction procedure are described in the Electronic Annex.

Overall, the correction to K_D^{exp} is relatively small, and is up to 0.2 log units for all HSEs investigated. After correction of the data, we do not see systematic differences

in partitioning of the HSEs when comparing experiments performed with different HSE-pairs and concentrations, which indicates that our correction procedure is reliable. In the following text we will refer to K_D^0(HSE) (infinite dilution) – the values of which are summarized in Table 1.

4.2. Effect of S concentration on HSE metal–silicate partitioning at 2473 K and 11 GPa

Overall, K_D^0(metal – silicate) values for all HSEs investigated were found to decrease with increasing S concentration in the Fe–FeS system, confirming that they are more siderophile than chalcophile (Fig. 2). This result is in agreement with solid metal – liquid metal partitioning behavior of the HSEs, where it was found that all HSEs prefer to partition into the S-free solid metal (Walker, 2000; Chabot and Jones, 2003). The extent to which K_D^0(metal – silicate) values decrease differs among the HSEs investigated (Fig. 2). While the effect on Pd (the least siderophile HSEs) of increasing X_S in the metal/sulfide phase is weak, it is strongest for Ir, which is the most siderophile of the HSEs. Thus, the K_D^0(metal – silicate) of all HSEs tend to converge as S concentrations become high, compared with S-free metal–silicate partitioning (Mann et al., 2012). The dependence of log K_D^0(metal – silicate) on X_S can be described by:

$$\log K_D^0(\text{metal} - \text{silicate}) = a^{met} + \frac{b^{met}}{T} + \frac{c^{met} * P}{T} + d^{met} \times \log(1 - X_S) \quad (11)$$

where T is in K and P in GPa. The constants a^{met}, b^{met}, c^{met} are related to the enthalpy, entropy and volume change of the exchange reaction respectively, whereas $d^{met} \times \log(1 - X_S)$ mimics the form of Margules parameter terms for the interaction with S in the metal or sulfide (e.g. Righter, 2011, and references therein).

The value of d^{met} was determined by fitting the isobaric and isothermal dataset (11 GPa and 2473 K) presented in this section (including S-free data of Mann et al., 2012) with the data weighted according to their uncertainties. The P and T dependence (parameters b^{met} and c^{met}) were taken from Mann et al. (2012). To generate an appropriate value for a^{met}, both datasets were fitted simultaneously with b^{met}, c^{met} and d^{met} fixed to the previously determined values. The fitting parameters resulting from this procedure are summarized in Table 2.

It is apparent from Fig. 2 that the decrease of log K_D^0(metal–silicate) with X_S is not linear over the entire range of S concentrations. Instead, all K_D^0(metal–silicate)

Table 1
Logarithmic values of metal–silicate and sulfide–silicate exchange coefficients (log K_D^0) for the HSEs corrected to infinite dilution (mol% basis).

Sample	P (GPa)	T (°C)	phase	Pt	±σ	Pd	±σ	Ru	±σ	Ir	±σ
H3729a	11	2473	met	5.37	±0.11			5.19	±0.26		
H3729b	11	2473	met	4.64	±0.02			4.21	±0.09		
H3738a	11	2473	met	4.84	±0.07	3.33	±0.03				
H3738b	11	2473	met	5.35	±0.02	3.58	±0.01				
H3788a	11	2473	met	5.25	±0.01			4.92	±0.15		
H3788b	11	2473	met	5.36	±0.03	3.39	±0.01				
H3820a	11	2473	sulf	4.22	±0.04	3.12	±0.02				
H3820b	11	2473	sulf	3.99	±0.04	3.17	±0.03				
Z989b	11	2473	met	4.92	±0.01			4.70	±0.11		
Z990a	11	2473	sulf	4.33	±0.02	3.20	±0.03				
Z990b	11	2473	sulf	4.04	±0.02	3.22	±0.02				
H3859a	11	2473	sulf			3.33	±0.02			4.41	±0.24
Z1014a	11	2473	sulf			3.21	±0.03			4.56	±0.16
Z1014b	11	2473	met			3.02	±0.01			4.62	±0.29
Z1110a	21	2473	sulf			3.19	±0.03			4.34	±0.17
Z1110b	21	2473	sulf	4.37	±0.02			3.63	±0.02		
H3980a	11	2373	sulf	4.25	±0.06	3.32	±0.05				
H3980b	11	2373	sulf	4.06	±0.04			4.18	±0.05		
H3985a	11	2673	sulf	3.95	±0.07	3.23	±0.05				
H3985b	11	2673	sulf	3.79	±0.04			3.50	±0.06		
H3986a	11	2573	sulf	4.01	±0.05			3.73	±0.08		
H4107a	11	2673	sulf			3.23	±0.02			4.03	±0.03
H4107b	11	2673	sulf	3.97	±0.01	3.34	±0.04				
H4138a	11	2373	sulf			3.28	±0.03			4.70	±0.08
H4138b	11	2373	sulf	4.14	±0.05			4.01	±0.06		
H4147b	7	2473	sulf	3.94	±0.04			3.84	±0.06		
Z1311a	7	2473	sulf			3.33	±0.07			4.39	±0.17
Z1311b	7	2473	sulf			3.24	±0.05				
H4184a	11	2473	sulf	4.23	±0.03			3.79	±0.03		
H4184b	11	2473	sulf			3.42	±0.03				

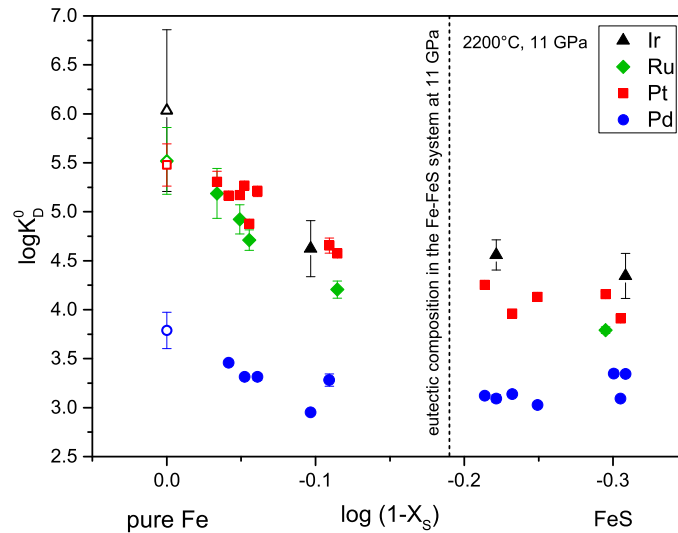All quoted uncertainties are 1σ standard deviation.

Fig. 2. Partitioning of the HSEs as a function of the mole fraction of S, expressed as $\log (1 - X_S)$ in the metal or sulfide phase. Open symbols are calculated from the regression for S-free metals presented by Mann et al. (2012), whereas closed symbols are data from this study. All log K_D^0 values (i.e. the HSE-Fe exchange coefficient corrected to infinite dilution) decrease with increasing X_S up to the eutectic composition in the Fe–FeS system (Fei et al., 1997; Buono and Walker, 2011).

Table 2
Results of the regression describing the dependence of log K_D^0 (metal − silicate) (corrected to infinite dilution) with P, T and X_S according to Eq. (11). The fit was restricted to Fe-rich metal compositions as described in the text ($X_S < 0.35$). Values for b^{met} and c^{met} are taken from Mann et al. (2012).

Element	a^{met}	$\pm\sigma$	b^{met}	$\pm\sigma$	c^{met}	$\pm\sigma$	d^{met}	$\pm\sigma$	n
Pt	−4.04	±0.04	23,824	±211	−17	±29	8.30	±3.65	16
Pd	0.18	±0.04	10,235	±126	−103	±25	9.08	±2.00	13
Ru	0.74	±0.05	12,760	±32	−63	±47	10.34	±1.29	12
Ir	−0.67	±0.13	17,526	±55	−19	±117	14.50	±4.80	9

values become relatively independent of S content at high S concentrations, above a value which coincides with the eutectic composition in the Fe–FeS system ($X_S \approx 0.35$ at 11 GPa – Fei et al., 1997; Buono and Walker, 2011). Therefore, we restricted our fit of Fe-rich metal compositions to $X_S < 0.35$. It is important to emphasize that the resulting equations should only be applied to Fe-rich metal compositions, i.e. with S concentrations less than that of the eutectic composition ($X_S \approx 0.35$ at 11 GPa).

Comparing our regression to results from three partitioning experiments presented by Righter et al. (2008) with up to 5 wt.% S in the metal shows, that their partition coefficients are lower by 1–1.5 log units. We attribute this discrepancy to compositional effects in the metallic melt. The metal employed by Righter et al. (2008) contains up to 6 wt.% Sn which may act to reduce the siderophile nature of the HSEs compared to our experiments.

4.3. Effect of P and T on FeS sulfide–silicate partitioning of the HSEs

The log K_D^0 (sulfide–silicate) values for all HSEs investigated are plotted in Fig. 3 as a function of inverse temperature (A) and pressure (B). It can be seen that K_D^0 (sulfide–silicate) for all HSEs decrease with increasing temperature although the effect on Pd is weak. With

increasing pressure K_D^0 (sulfide–silicate) values for Ru, Pd and Ir decrease while that of Pt increases. The effects of T and P on K_D^0 (sulfide–silicate) can be expressed by:

$$\log K_D^0(\text{sulfide} - \text{silicate}) = a^{sulf} + \frac{b^{sulf}}{T} + \frac{c^{sulf} \times P}{T} \quad (12)$$

where a^{sulf}, b^{sulf} and c^{sulf} are constants specific to each element (cf. Section 4.2), T is given in K and P in GPa. We have fitted the T-dependence of HSE partitioning between sulfide liquid and peridotite melt using isobaric data (11 GPa) from our study. Subsequently, the P-dependence was fitted to the complete dataset with b^{sulf} fixed to the value obtained in the first step. The results of the fitting procedure are summarized in Table 3.

The results highlight an interesting feature of the sulfide–silicate system. At pressures above ~20 GPa Pt becomes more chalcophile than Ru. From this it follows that Ru is more lithophile at high pressures compared to Pt, which is different to the metal–silicate system where Ru is always more siderophile than Pt (Mann et al., 2012).

4.4. Sulfur concentration at sulfide saturation (SCSS) for silicate melt with primitive mantle composition

Sulfur dissolves as the S^{2-} anion in silicate melts by replacing O^{2-} anions, provided the conditions are
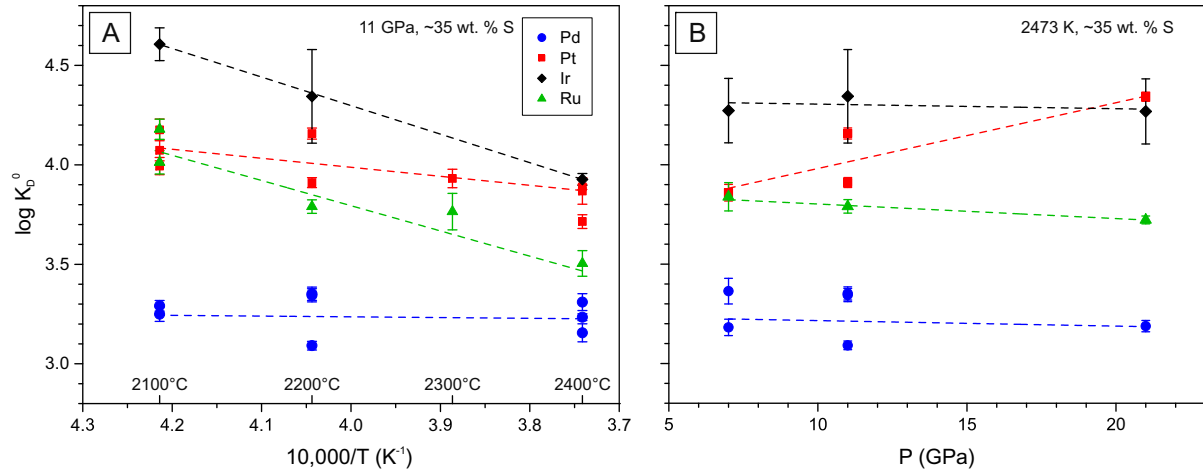
Fig. 3. Partitioning of HSEs between sulfide and peridotite liquids. Logarithmic values of the exchange coefficient K_D^0 (corrected to infinite dilution) of the HSEs are plotted as a function of inverse temperature (A) and pressure (B).

Table 3
Results of the regression describing the dependence of log K_D^0 (sulfide–silicate) (corrected to infinite dilution) on P and T.

Element	a^{sulf}	$\pm\sigma$	b^{sulf}	$\pm\sigma$	c^{sulf}	$\pm\sigma$	n
Pt	2.04	±0.10	4306	±1638	69.4	±20.9	11
Pd	3.02	±0.09	842	±1653	−19.1	±17.7	11
Ru	−1.13	±0.12	12,748	±2730	−41.4	±25.2	7
Ir	−1.16	±0.06	14,073	±314	−17.8	±13.1	5

sufficiently reduced (i.e. below ∼FMQ – e.g. Jugo et al., 2005, 2010; Métrich et al., 2009). As outlined in detail by Mavrogenes and O'Neill (1999) the concentration of sulfur in a silicate melt saturated with molten FeS sulfide is independent of fO_2 and fS_2, but is a function of pressure and temperature (Fincham and Richardson, 1954; Mavrogenes and O'Neill, 1999). If the composition of the silicate melt is constant, SCSS can be expressed as:

$$\ln(S)_{SCSS} = a^{SCSS} + \frac{b^{SCSS}}{T} + \frac{c^{SCSS} \times P}{T} + \ln(a_{FeS}^{sulfide}) \quad (13)$$

where the concentration of S is given in ppm, T is in K and P in GPa. The parameters a^{SCSS}, b^{SCSS} and c^{SCSS} are constants that can be determined experimentally.

SCSS is a strong function of silicate melt composition, especially its FeO concentration (Haughton et al., 1974; O'Neill and Mavrogenes, 2002; Li and Ripley, 2005, 2009; Fortin et al., 2015; Wykes et al., 2015; Namur et al., 2016) which implies that S dissolves as Fe–S complexes in silicate melts. This was confirmed by identifying Fe–S bonds within silicate glasses using Raman-spectroscopy (Klimm and Botcharnikov, 2010). Therefore, the fitting parameters need to be determined individually for different melt compositions. This has been done for several melt compositions such as basalts and andesites (e.g. Mavrogenes and O'Neill, 1999), but corresponding data for primitive mantle compositions are not available. Empirical models describing SCSS as a function of P–T and melt composition are available in the literature (e.g. Li and Ripley, 2009; Fortin et al., 2015; Namur et al., 2016). However, these parameterizations include only very few data at

pressures higher than 3 GPa. The effect of silicate melt composition on SCSS at high P and T is not constrained, thus preventing the direct application of these models to our dataset. Therefore, we adopted the formalism by Mavrogenes and O'Neill (1999) to describe SCSS for a primitive mantle composition using the S concentrations measured in silicate melts of the sulfide-saturated experiments presented in Section 4.3 (concentration of FeO = 7.2 ± 1.5 wt.% – Table EA1). In addition, we also included S concentration data from sulfide–silicate siderophile element partitioning experiments at high P and T from Vogel (2015). Fitting these S concentrations to Eq. (13) with the data weighted according to their uncertainties and assuming $a_{FeS}^{sulfide} \approx 1$ (c.f. Mavrogenes and O'Neill, 1999) gives:

$$\ln(S)_{SCSS} = 14.2(\pm 1.18) + \frac{-11032(\pm 3119)}{T}$$
$$+ \frac{-379(\pm 82) \times P}{T} \quad (14)$$

The obtained fitting parameters are within the range of values reported by Mavrogenes and O'Neill (1999). In detail, however, SCSS for peridotite melt is significantly higher than for CV3 (Allende) chondritic or basaltic melts (Li and Agee, 1996; Mavrogenes and O'Neill, 1999) at pressures up to ∼20 GPa (Fig. 4, with T fixed approximately midway between the peridotite liquidus and solidus – Rubie et al., 2015). The differences in SCSS are most likely due to the different silicate melt compositions of the three studies. Considering the work by O'Neill and Mavrogenes (2002) who investigated in detail the effect of melt
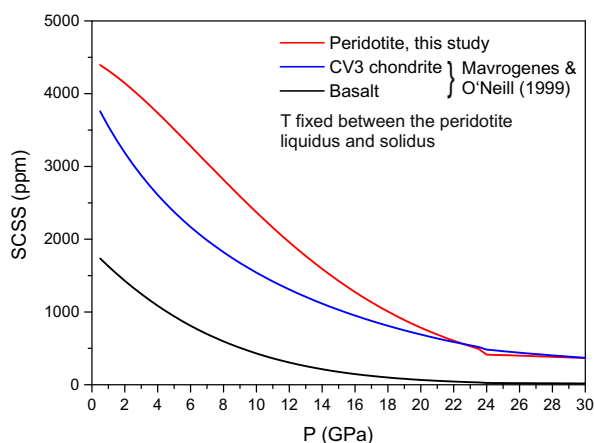
Fig. 4. Comparison of the sulfur content at sulfide saturation (SCSS) for different silicate melt compositions as a function of pressure. The temperature is fixed approximately midway between the peridotite liquidus and solidus as defined by Rubie et al. (2015). Below ~20 GPa SCSS in peridotite melt is significantly higher than in basalts or CV3 chondrite (Mavrogenes and O'Neill, 1999), while above ~20 GPa SCSS for peridotite and CV3 compositions converge.

composition at 1 bar and 1673 K, the higher SCSS for peridotite compared to basalt is consistent with the general differences expected from their melt compositions. Using the parameterization presented by O'Neill and Mavrogenes (2002) SCSS can be computed as a function of silicate melt composition at 1673 K and 1 bar. At these conditions, we calculated SCSSs of ~2250 ppm S for basaltic melt and ~4800 ppm S for the average peridotite composition of our experiments, broadly consistent with our experimental observations. This is not true when comparing peridotite and CV3 chondrite which have broadly similar compositions as peridotite except for the twofold higher FeO concentration in the CV3 melt. This higher FeO concentration would imply higher SCSS for CV3 (~7850 ppm S at 1673 K and 1 bar) than for peridotite. This is opposite to what we observe in our experiments and is also not reflected by the parameterization of Mavrogenes and O'Neill (1999) which predicts ~4000 ppm S. However, sulfides present in the experiments of Li and Agee (1996), on which the CV3 fit is based, have less than 30 wt.% S compared to 36 wt.% S of a stoichiometric FeS melt, which results in $a_{FeS} < 1$ and may be the reason for the lower S-concentration observed in their experiments. Also, the T-dependence of SCSS for CV3 melts is unknown as the experiments by Li and Agee (1996) were performed at a single temperature (2273 K). Therefore, the b/T-term (cf. Eq. (13)) was omitted from the parameterization for CV3 by Mavrogenes and O'Neill (1999). Ignoring the effect of T will certainly lead to significant deviations from the true value when calculating SCSS. Despite some discrepancies with previous results we are confident that SCSS for primitive mantle composition is well described by our parameterization, since we included data from two independent but consistent datasets and determined the regression parameters specifically for a primitive mantle melt composition.

5. DISCUSSION

5.1. Modeling the behavior of HSEs and S during the formation of Earth's core

In order to understand how the HSE abundances of the Earth's mantle were established, we have modeled the partitioning of the HSEs and S in a simple 2-stage core-formation model using our newly-determined metal–silicate and sulfide–silicate exchange coefficients and SCSS as parameterized in the previous section. Our calculations are based on the model presented by O'Neill (1991) and adopt a CI chondrite composition for HSEs for Earth's building blocks (Fischer-Gödde et al., 2010; Palme and O'Neill, 2014). We assume that the proto-Earth (90% of the final Earth mass M_E) is accreted from reduced and volatile-depleted material which is essentially S-free. In this first stage (Step 1) the partitioning of the HSEs is modeled under strongly reducing conditions at IW-4 (Frost et al., 2008) using the metal–silicate partitioning expressions presented by Mann et al. (2012). Metal–silicate equilibration takes place over a range of pressures as iron droplets sink to the core so we defined an "effective" equilibration pressure, which reflects the cumulative effects of partitioning over a range of P–T conditions (e.g. Rubie et al., 2003). We assume that equilibration occurs effectively at a constant fraction of the pressure at the core-mantle boundary (CMB) of $P_{eq}^{metal–silicate} = 0.33 \times P_{CMB}$ (e.g. Wade and Wood, 2005; Wood et al., 2014) with T being fixed approximately midway between the peridotite liquidus and solidus (Rubie et al., 2015). The HSE abundances of the Earth's mantle were calculated by mass balance assuming for simplicity that the core comprises 16.6 mol % (~32 wt.%) of the proto-Earth, equal to the present-day core mass fraction, and equilibrates with the entire silicate mantle (83.4 mol% ≈ 68 wt.%). As expected, core formation results in strongly depleted and fractionated HSE abundances in the Earth's mantle (c.f. Mann et al., 2012).

After this episode of core formation, more oxidized and volatile-rich material (CI composition in HSEs and S) was accreted (about 10% M_E) which O'Neill (1991) associated with the Moon-forming impact. The accreted material was mixed with the entire silicate mantle and the oxidation state of the mantle is raised to IW-2 (Frost et al., 2008). Again, the fraction of metal segregating to the core is taken to be 16.6 mol% of the impactor, which translates into ~1.9 mol% of the mantle after the addition of the more oxidized material (10% M_E). The abundances of S in the core-forming metal and silicate magma ocean are calculated via mass balance on the basis of high P–T metal–silicate partition coefficients for S as parameterized by Boujibar et al. (2014) (Step 2a). As in Step 1, we assume that equilibration takes place at $P_{eq}^{metal–silicate} = 0.33 \times P_{CMB}$. The inferred S concentration of the metal ($X_S = 17$ mol%) is then used to model the metal–silicate partitioning of the HSEs using the S-bearing metal–silicate partitioning data presented in Section 4.2. Since the presence of S in the metal substantially lowers metal–silicate partition coefficients of the HSEs, the resulting HSE abundances in the mantle are shifted to higher values compared to the first

S-free stage of core-formation (Fig. 5). Nevertheless, HSE abundances are 2 to 3 orders of magnitude smaller than concentrations estimated for PUM (Becker et al., 2006; Barnes et al., 2015) except for Pd which is the least siderophile of the HSEs.

After this second phase of metal segregation ~420 ppm S remain in the magma ocean. Since S-solubility in silicate melts is a strong function of P and T (cf. Section 4.4, e.g. Mavrogenes and O'Neill, 1999) the magma ocean will be oversaturated with respect to FeS sulfide melt at pressures above ~24 GPa (T fixed between peridotite liquidus and solidus). An immiscible sulfide melt ("Hadean matte") will exsolve pervasively from the magma ocean and equilibrates with the silicate melt upon exsolution (cf. Laurenz et al., 2013). Due to its high density, the sulfide liquid segregates to the core. We calculate the fraction of sulfide to be ~0.2 mol% of the mantle, based on SCSS in peridotite melts (section 4.4) and on the S concentration in the magma ocean (420 ppm). The abundances of HSEs in the mantle are modeled using the P–T dependence of sulfide–silicate partitioning as presented in Section 4.3 (Step 2b). Segregation of sulfide melt to the core results in further depletion of the mantle in HSEs and S (Fig. 5). Sulfide–silicate equilibration produces different HSE patterns in the mantle compared to metal–silicate equilibration: Pt becomes more depleted than Ru, since Ru is less chalcophile at high P–T.

This late stage sulfide segregation is followed by a late veneer (CI chondrite composition), which is homogenized with the entire silicate mantle (Step 3). We estimate that 0.6% M_E of material was added to the Earth's mantle, which is consistent with previous estimates ranging from 0.3% to 1% (e.g. Morgan et al., 2001; Walker, 2009; Jacobson et al., 2014). The model described in this section will be referred to as model M1.
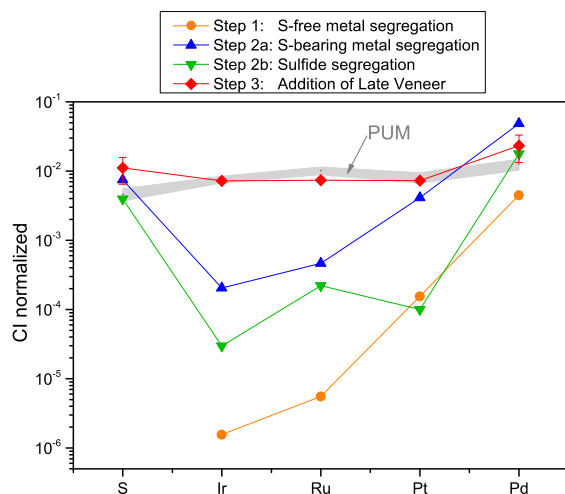

Fig. 5. Evolution of HSE abundances in Earth's mantle during model M1 ($P_{eq}^{metal-silicate} = 0.33 \times P_{CMB}$, $P_{eq}^{sulfide-silicate} = 0.33 \times P_{CMB}$). For comparison, HSE abundances estimated for PUM are shown by the gray band (HSEs: Becker et al., 2006; S: McDonough and Sun, 1995).

5.2. HSE and S mantle abundances

Overall, HSE abundances in PUM (Becker et al., 2006; Barnes et al., 2015) are reproduced fairly well by our model calculations (Fig. 5). Palladium remains in the mantle in substantial amounts at all stages during accretion and core formation, so that resulting Pd/Ir ratios in the final mantle are suprachondritic in agreement with the current estimates for PUM (Becker et al., 2006; Barnes et al., 2015). However, this is not the case for Ru/Ir, which is also considered to be suprachondritic in PUM. Although the mantle exhibits elevated Ru/Ir as a result of sulfide segregation, the addition of the late veneer erases these pre-existing fractionations and the suprachondritic Ru/Ir of PUM is not reproduced.

In order to better reproduce the Ru/Ir of PUM, we adjusted our model such that after the accretion of volatile-rich material and subsequent Fe-metal segregation under S-bearing conditions (Step 2a in model M1), another 1% of material (CI chondrite composition) was accreted to the mantle. This material was mixed with the entire mantle replenishing the HSEs and S and resulting in the exsolution and segregation of an immiscible FeS-sulfide melt (O'Neill, 1991; Ballhaus et al., 2013). In contrast to M1 the mantle is replenished in HSEs before sulfide segregation occurs. The P–T conditions of sulfide–silicate equilibration remain the same as in M1 (i.e. $P_{eq}^{metal-silicate} = 0.33 \times P_{CMB}$, $P_{eq}^{sulfide-silicate} = 0.33 \times P_{CMB}$). Again, late-stage sulfide segregation is followed by accretion of a late veneer (0.6% M_E, CI chondrite composition). As can be seen in Fig. 6, M2 yields slightly suprachondritic Ru/Ir and considerably suprachondritic Pd/Ir in the mantle, showing that sulfide segregation is potentially the key to explaining the abundances and ratios of HSEs in PUM. This second model will be termed M2 in the following text.

A problem is that in both models M1 and M2 the resulting S-abundances in the mantle (~600 ppm S) are too large compared to current estimates for PUM, although PUM values are not well constrained (~200–250 ppm – McDonough and Sun, 1995; Palme and O'Neill, 2014). One possibility for generating smaller S abundances is to increase the pressure of sulfide–silicate equilibration, as higher pressures result in lower SCSS in the magma ocean. If the equilibration pressure of the final episode of sulfide–silicate segregation is increased to $P_{eq}^{sulfide-silicate} = 0.5 \times P_{CMB}$, a smaller amount of late veneer (~0.4% M_E) is necessary to account for the mantle's HSE abundances (model M3) because Ir and Ru then become less chalcophile. Resulting concentrations of Pt in the final mantle are slightly low (4.6 ng/g or ppb) compared to current estimates for PUM (6.2–7.3 ppb – Becker et al., 2006; Barnes et al., 2015). However, given the simplified nature of our core formation model, this discrepancy should be acceptable.

Uncertainties on the final mantle concentrations were calculated by propagating the uncertainties on the fitting parameters (i.e. the partition coefficients) at each step of the model calculations. Uncertainties on the composition of the CI chondrites were not taken into account. As can be seen in Fig. 6 the uncertainty calculated for the final
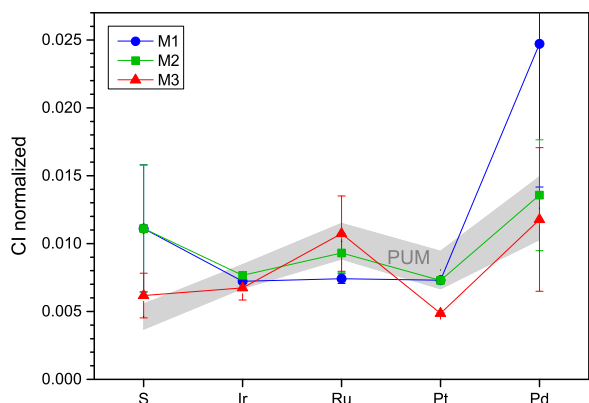
Fig. 6. Comparison of models M1 and M2 ($P_{eq}^{metal-silicate} = 0.33 \times P_{CMB}$, $P_{eq}^{sulfide-silicate} = 0.33 \times P_{CMB}$) with M3 ($P_{eq}^{metal-silicate} = 0.33 \times P_{CMB}$, $P_{eq}^{sulfide-silicate} = 0.5 \times P_{CMB}$). HSE and S abundances of PUM (HSEs: Becker et al., 2006; S: McDonough and Sun, 1995) can only be reproduced simultaneously if late stage sulfide segregation occurs from a mantle with substantial HSE abundances (M3). See main text for details.
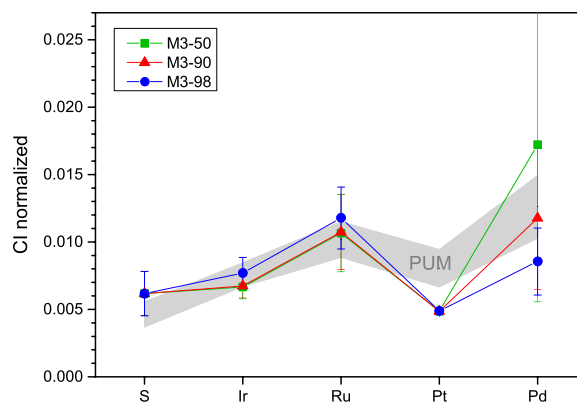
Fig. 7. Comparison of results for model M3 ($P_{eq}^{metal-silicate} = 0.33 \times P_{CMB}$, $P_{eq}^{sulfide-silicate} = 0.5 \times P_{CMB}$) in which the timing of S-addition is varied. The number in the legend denotes the timing of S-addition for the specific model (e.g. in model M3-50 sulfur was added after 50% of accretion). The results for all three compositions agree reasonably well with the current estimates for PUM (Becker et al., 2006; S: McDonough and Sun, 1995).

Pt concentration of Earth's mantle is small. This reflects the fact that the mantle is essentially devoid of Pt after core formation and Pt is almost entirely derived from the late veneer, which we assume to be without uncertainty in our error propagation. Therefore, uncertainties on the partition coefficients do not contribute significantly to the uncertainty calculated for Pt. In contrast, Pd and Ru exhibit larger error bars, because some Pd and Ru remain in the mantle after core formation. Uncertainties for Pd and Ru therefore reflect the uncertainties in the experimentally determined partition coefficients.

The modeled S concentration of the mantle is then 332 ± 87 ppm, which reproduces the current estimates for PUM within error (Fig. 6). Hence, the HSE and S signature of the Earth's mantle can be envisioned as a compound signature which arises from the segregation of a FeS sulfide melt at high P–T from a mantle with substantial HSE concentrations in combination with the addition of a late veneer (CI composition in model M3) after sulfide segregation ceased.

5.3. Timing of volatile addition

There is an ongoing debate as to when sulfur and other volatile elements were accreted to Earth. Based on accretion dynamics, it has been argued that water, and by analogy other volatiles such as S, were accreted continuously during Earth's accretion and concentrations in the proto-mantle became significant after 60–80% of its final mass has accreted (O'Brien et al., 2014; Rubie et al., 2015). Other models favor later addition of volatiles and sulfur, either during the last 10–20% of accretion similar to our model (O'Neill, 1991; Wade et al., 2012; Wood et al., 2014), or by the late veneer only (Albarede, 2009; Marty, 2012; Ballhaus et al., 2013). We have tested these possibilities by adjusting the timing of S-addition in our model. In addition to model M3, where S is added after 90% of accretion (M3-90), we have also examined two scenarios where S is

added after 50% of accretion (model M3-50) and after 98% of accretion (model M3-98). Comparing the results of these models shows that all three can reproduce the HSEs in PUM equally well, regardless of whether S is added after 50% of accretion, or only after 98%, although the model results for Ir and Ru are slightly larger than PUM in the latter case (Fig. 7). Thus, in terms of reproducing the HSE abundances of the Earth's mantle, the timing of S-addition to the Earth's mantle is irrelevant. The key to producing a good fit for HSE mantle abundances is that a final episode of sulfide segregation must have occurred from a mantle with non-negligible HSE abundances (modeled by the addition of a small amount of CI chondrite material to the mantle previously depleted in HSE by metal segregation) combined with the addition of a late veneer.

5.4. Composition of Earth's building blocks and the late veneer

We assumed that Earth was accreted from material with a CI chondrite composition in our model. However, there is evidence that Earth's bulk composition is similar isotopically to enstatite chondrites (Javoy et al., 2010), in agreement with the Os- and Ru isotopic composition of the mantle (Meisel et al., 2001; Brandon et al., 2006; Fischer-Gödde et al., 2015; Walker et al., 2015). Therefore, we repeated our model assuming Earth was accreted from material with two different enstatite chondrite compositions (models M3-EH and M3-EL). We used S concentrations from Wasson and Kallemeyn (1988) (EH: 5.8 wt.% S; EL: 3.3. wt.% S), whereas HSE abundances are from Horan (2003) and Fischer-Gödde et al. (2010). All other parameters are as in model M3 (i.e. $P_{eq}^{metal-silicate} = 0.33 \times P_{CMB}$, $P_{eq}^{sulfide-silicate} = 0.5 \times P_{CMB}$ and the fraction of late veneer is 0.4% M_E). Using enstatite chondrite composition, the modeled mantle abundances of the HSEs are higher compared to using CI chondrite (Fig. 8). This can be attributed to overall higher HSE concentrations in enstatite chondrites
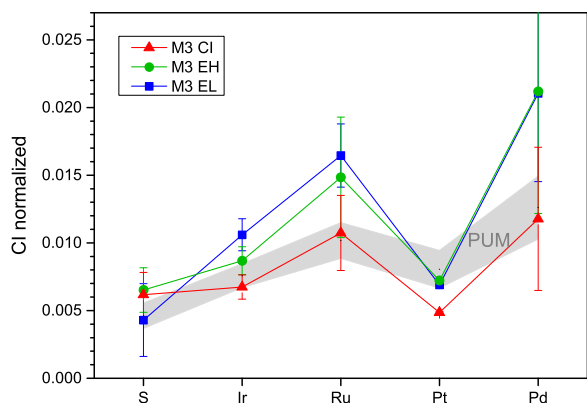
Fig. 8. Comparison of results for model M3 ($P_{eq}^{metal–silicate} = 0.33 \times P_{CMB}$, $P_{eq}^{sulfide–silicate} = 0.5 \times P_{CMB}$) using CI, EH and EL chondrite compositions for HSEs and S (Wasson and Kallemeyn, 1988; Horan, 2003; Fischer-Gödde et al., 2010; Palme and O'Neill, 2014) for Earth's building blocks. The results for CI and EH chondrite compositions agree reasonably well with the current estimates for PUM (HSEs: Becker et al., 2006; S: McDonough and Sun, 1995). Using EL or EH compositions result in slightly higher abundances for the HSEs, which could be fixed by reducing the amount of late veneer.

compared to CI. Differences between EL and EH chondrite are due to lower S concentration in EL compared to EH, thus leading to a smaller amount of sulfide exsolving and segregating to the core. Using enstatite chondrite, the modeled abundances of Ru, Ir, Pd are slightly high compared to PUM, which could, of course, be adjusted by reducing the amount of late veneer added to Earth's mantle or varying the $P–T$ conditions used in each step of the model.

In order to reconcile suprachondritic Ru/Ir and Pd/Ir ratios as well as Os-isotope signatures in the Earth's mantle and lunar impact melt rocks with chondritic Se–Te abundances in Earth's mantle, it has recently been advocated that the late veneer was composed either of a mixture of CI-chondrite material with iron-meteorite-like material (e.g. Fischer-Gödde and Becker, 2012; Kruijer et al., 2015) or of material currently not present in the meteorite collection (Wang and Becker, 2013; Fischer-Gödde et al., 2015; Walker et al., 2015). In contrast, the results of our model show that the elevated Ru/Ir and Pd/Ir ratios of the mantle can also be generated by a planetary process, namely the late stage sulfide segregation from a mantle with substantial HSE concentrations in combination with a late veneer of 0.4% M_E.

6. SUMMARY AND CONCLUSIONS

The results of our experimental study on the metal–silicate partitioning of the HSEs show that all HSEs investigated here become less siderophile with increasing concentrations of S in the metal. Therefore, if core-forming metal contains S, it will be less efficient in extracting the HSEs to the core than S-free metal. Furthermore, our results for the sulfide–silicate partitioning of the HSEs show that the same HSEs become less chalcophile with increasing temperature. With increasing pressure Ru, Ir and Pd become less chalcophile, whereas the effect is

opposite for Pt, which becomes significantly more chalcophile. The net result is that at high $P–T$ conditions Ru is less chalcophile than Pt, which is opposite to what is observed in metal–silicate partitioning experiments.

We have modeled the partitioning of the HSEs and S in a simple core formation model, including a newly-determined $P–T$ dependence of SCSS for peridotite melt. Our model shows, that HSE abundances of the Earth's mantle can be well reproduced, if segregation of a late-stage sulfide melt ("Hadean matte") to the core is taken into account. Importantly, this sulfide melt must equilibrate with a mantle with substantial HSE concentrations (modeled by the addition of a small amount of chondritic material) in order to reproduce the suprachondritic Ru/Ir and Pd/Ir ratios estimated for the Earth's mantle.

Open questions remain, especially on the composition of the late veneer. Late-stage sulfide segregation provides a solution to reconciling the HSE abundances of the mantle with CI-chondrite-like composition of the late veneer, which is required by Se–Te abundances of the mantle (Wang and Becker, 2013). However, the Os-isotope signature of the mantle is more consistent with that of ordinary or enstatite chondrites (e.g. Meisel et al., 2001). Our model reproduces the mantle well with either composition for Earth's building blocks. Whether the Re/Os ratio and Os-isotope signature of the mantle are in agreement with our model will become apparent, once high $P–T$ sulfide–silicate partitioning data are available for Re and Os.

Although our simple model is able to reproduce the concentrations of the HSEs and S of the Earth's mantle and suprachondritic Pd/Ir and Ru/Ir ratios, it does not reflect the complexity of Earth's accretion and core formation history. Dynamical models show, that accretion took place via multiple impacts, resulting in multiple core-formation events (O'Brien et al., 2006; Rubie et al., 2011, 2015; Walsh et al., 2011). These will have involved metal–silicate equilibration as well as sulfide–silicate equilibration with increasing depth over time. Also processes such as incomplete equilibration (e.g. Rubie et al., 2011) or core merging were not taken into account. Modeling the behavior of the HSEs and S in a combined accretion and core-formation model by Rubie et al. (2016) shows that contrary to our simple model metal-silicate equilibration leads to an increase in HSE and S abundances of the Earth's mantle. This model confirms that segregation of a sulfide liquid to the core is essential to reproduce manlte HSE and S abuncances.

APPENDIX A. SUPPLEMENTARY DATA

Supplementary data associated with this article can be found, in the online version, at http://dx.doi.org/10.1016/j.gca.2016.08.012.

REFERENCES

Albarede F. (2009) Volatile accretion history of the terrestrial planets and dynamic implications. *Nature* **461**, 1227–1233.

Ballhaus C., Laurenz V., Münker C., Fonseca R. O., Albarède F., Rohrbach A., Lagos M., Schmidt M. W., Jochum K.-P., Stoll B., Weis U. and Helmy H. M. (2013) The U/Pb ratio of the Earth's mantle—A signature of late volatile addition. *Earth Planet. Sci. Lett.* **362**, 237–245.

Barnes S. J., Mungall J. E. and Maier W. D. (2015) Platinum group elements in mantle melts and mantle samples. *Lithos* **232**, 395–417.

Becker H., Horan M. F., Walker R. J., Gao S., Lorand J. P. and Rudnick R. L. (2006) Highly siderophile element composition of the Earth's primitive upper mantle. *Geochim. Cosmochim. Acta* **70**, 4528–4550.

Bezmen N. I., Asif M., Brügmann G. E., Romanenko I. M. and Naldrett A. J. (1994) Distribution of Pd, Rh, Ru, Ir, Os, and Au between sulfide and silicate metals. *Geochim. Cosmochim. Acta* **58**, 1251–1260.

Borisov A. and Palme H. (2000) Solubilities of noble metals in Fe-containing silicate melts as derived from experiments in Fe-free systems. *Am. Mineral.* **85**, 1665–1673.

Botcharnikov R. E., Linnen R. L. and Holtz F. (2010) Solubility of Au in Cl- and S-bearing hydrous silicate melts. *Geochim. Cosmochim. Acta* **74**, 2396–2411.

Boujibar A., Andrault D., Bouhifd M. A., Bolfan-Casanova N., Devidal J.-L. and Trcera N. (2014) Metal–silicate partitioning of sulphur, new experimental and thermodynamic constraints on planetary accretion. *Earth Planet. Sci. Lett.* **391**, 42–54.

Brandon A. D., Walker R. J. and Puchtel I. S. (2006) Platinum-osmium isotope evolution of the Earth's mantle: constraints from chondrites and Os-rich alloys. *Geochim. Cosmochim. Acta* **70**, 2093–2103.

Brenan J. M. (2015) Se–Te fractionation by sulfide–silicate melt partitioning: implications for the composition of mantle-derived magmas and their melting residues. *Earth Planet. Sci. Lett.* **422**, 45–57.

Brenan J. M. and McDonough W. F. (2009) Core formation and metal–silicate fractionation of osmium and iridium from gold. *Nat. Geosci.* **2**, 798–801.

Buono A. S. and Walker D. (2011) The Fe-rich liquidus in the Fe–FeS system from 1 bar to 10 GPa. *Geochim. Cosmochim. Acta* **75**, 2072–2087.

Chabot N. L. and Agee C. B. (2003) Core formation in the Earth and Moon: new experimental constraints from V, Cr, and Mn. *Geochim. Cosmochim. Acta* **67**, 2077–2091.

Chabot N. L. and Drake M. J. (1997) An experimental study of silver and palladium partitioning between solid and liquid metal, with applications to iron meteorites. *Meteorit. Planet. Sci.* **32**, 637–645.

Chabot N. L. and Jones J. H. (2003) The parameterization of solid metal–liquid metal partitioning of siderophile elements. *Meteorit. Planet. Sci.* **38**, 1425–1436.

Chabot N. L., Campbell A. J., Jones J. H., Humayun M. and Agee C. B. (2003) An experimental test of Henry's Law in solid metal–liquid metal systems with implications for iron meteorites. *Meteorit. Planet. Sci.* **38**, 181–196.

Chabot N. L., Saslow S. A., McDonough W. F. and McCoy T. J. (2007) The effect of Ni on element partitioning during iron meteorite crystallization. *Meteorit. Planet. Sci.* **42**, 1735–1750.

Chabot N. L., Saslow S. A., McDonough W. F. and Jones J. H. (2009) An investigation of the behavior of Cu and Cr during iron meteorite crystallization. *Meteorit. Planet. Sci.* **44**, 505–519.

Corgne A., Keshav S., Wood B. J., McDonough W. F. and Fei Y. W. (2008) Metal–silicate partitioning and constraints on core composition and oxygen fugacity during Earth accretion. *Geochim. Cosmochim. Acta* **72**, 574–589.

Cottrell E., Kelley K. A., Lanzirotti A. and Fischer R. A. (2009) High-precision determination of iron oxidation state in silicate glasses using XANES. *Chem. Geol.* **268**, 167–179.

Crocket J. H., Fleet M. E. and Stone W. E. (1997) Implications of composition for experimental partitioning of platinum-group elements and gold between sulfide liquid and basalt melt: the significance of nickel content. *Geochim. Cosmochim. Acta* **61**, 4139–4149.

Dale C. W., Burton K. W., Greenwood R. C., Gannoun A., Wade J., Wood B. J. and Pearson D. G. (2012) Late accretion on the earliest planetesimals revealed by the highly siderophile elements. *Science* **336**, 72–75.

Day J. M. D., Pearson D. G. and Taylor L. A. (2007) Highly siderophile element constraints on accretion and differentiation of the Earth–Moon system. *Science* **315**, 217–219.

Ertel W., Walter M. J., Drake M. J. and Sylvester P. J. (2006) Experimental study of platinum solubility in silicate melt to 14 GPa and 2273 K. *Geochim. Cosmochim. Acta* **70**, 2591–2602.

Ertel W., Dingwell D. B. and Sylvester P. J. (2008) Siderophile elements in silicate melts – A review of the mechanically assisted equilibration technique and the nanonugget issue. *Chem. Geol.* **248**, 119–139.

Fei Y., Bertka C. M. and Finger L. W. (1997) High-pressure iron–sulfur compound, Fe3S2, and melting relations in the Fe–FeS System. *Science* **275**, 1621–1623.

Fincham C. J. B. and Richardson F. D. (1954) The behaviour of sulphur in silicate and aluminate melts. *Proc. R. Soc. A* **223**, 40–62.

Fischer R. A., Nakajima Y., Campbell A. J., Frost D. J., Harries D., Langenhorst F., Miyajima N., Pollok K. and Rubie D. C. (2015) High pressure metal–silicate partitioning of Ni Co, V, Cr, Si, and O. *Geochim. Cosmochim. Acta* **167**, 177–194.

Fischer-Gödde M. and Becker H. (2012) Osmium isotope and highly siderophile element constraints on ages and nature of meteoritic components in ancient lunar impact rocks. *Geochim. Cosmochim. Acta* **77**, 135–156.

Fischer-Gödde M., Becker H. and Wombacher F. (2010) Rhodium, gold and other highly siderophile element abundances in chondritic meteorites. *Geochim. Cosmochim. Acta* **74**, 356–379.

Fischer-Gödde M., Burkhardt C., Kruijer T. S. and Kleine T. (2015) Ru isotope heterogeneity in the solar protoplanetary disk. *Geochim. Cosmochim. Acta* **168**, 151–171.

Fleet M. E., Stone W. E. and Crocket J. H. (1991) Partitioning of palladium, iridium, and platinum between sulfide liquid and basalt melt. *Geochim. Cosmochim. Acta* **55**, 2545–2554.

Fonseca R. O., Campbell I. H., St. O'Neill H. C. and Allen C. M. (2009) Solubility of Pt in sulphide mattes. *Geochim. Cosmochim. Acta* **73**, 5764–5777.

Fonseca R. O., Mallmann G., O'Neill H. S., Campbell I. H. and Laurenz V. (2011) Solubility of Os and Ir in sulfide melt. *Earth Planet. Sci. Lett.* **311**, 339–350.

Fonseca R. O., Laurenz V., Mallmann G., Luguet A., Hoehne N. and Jochum K. P. (2012) New constraints on the genesis and long-term stability of Os-rich alloys in the Earth's mantle. *Geochim. Cosmochim. Acta* **87**, 227–242.

Fortenfant S. S., Gunther D., Dingwell D. B. and Rubie D. C. (2003) Temperature dependence of Pt and Rh solubilities in a haplobasaltic melt. *Geochim. Cosmochim. Acta* **67**, 123–131.

Fortenfant S. S., Dingwell D. B., Ertel-Ingrisch W., Capmas F., Birck J. L. and Dalpe C. (2006) Oxygen fugacity dependence of Os solubility in haplobasaltic melt. *Geochim. Cosmochim. Acta* **70**, 742–756.

Fortin M.-A., Riddle J., Desjardins-Langlais Y. and Baker D. R. (2015) The effect of water on the sulfur concentration at sulfide saturation (SCSS) in natural melts. *Geochim. Cosmochim. Acta* **160**, 100–116.

Frost D., Poe B., Trønnes R., Liebske C., Duba A. and Rubie D. (2004) A new large-volume multianvil system. *Phys. Earth Planet Inter.* **143–144**, 507–514.

Frost D., Mann U., Asahara Y. and Rubie D. (2008) The redox state of the mantle during and just after core formation. *Philos. Trans. R. Soc. Assoc.* **366**, 4315–4337.

Geßmann C. K. and Rubie D. C. (1998) The effect of temperature on the partitioning of nickel, cobalt, manganese, chromium, and vanadium at 9 GPa and constraints on formation of the Earth's core. *Geochim. Cosmochim. Acta* **62**, 867–882.

Haughton D. R., Roeder P. L. and Skinner B. J. (1974) Solubility of sulfur in mafic magmas. *Econ. Geol.* **69**, 451–467.

Holzheid A., Sylvester P., O'Neill H. S. C., Rubie D. C. and Palme H. (2000) Evidence for a late chondritic veneer in the Earth's mantle from high-pressure partitioning of palladium and platinum. *Nature* **406**, 396–399.

Horan M. (2003) Highly siderophile elements in chondrites. *Chem. Geol.* **196**, 27–42.

Jacobson S. A., Morbidelli A., Raymond S. N., O'Brien D. P., Walsh K. J. and Rubie D. C. (2014) Highly siderophile elements in Earth's mantle as a clock for the Moon-forming impact. *Nature* **508**, 84.

Jana D. and Walker D. (1997a) The influence of sulfur on partitioning of siderophile elements. *Geochim. Cosmochim. Acta* **61**, 5255–5277.

Jana D. and Walker D. (1997b) The impact of carbon on element distribution during core formation. *Geochim. Cosmochim. Acta* **61**, 2759–2763.

Javoy M., Kaminski E., Guyot F., Andrault D., Sanloup C., Moreira M., Labrosse S., Jambon A., Agrinier P., Davaille A. and Jaupart C. (2010) The chemical composition of the Earth. *Earth Planet. Sci. Lett.* **293**, 259–268.

Jochum K. P., Weis U., Stoll B., Kuzmin D., Yang Q., Raczek I., Jacob D. E., Stracke A., Birbaum K., Frick D. A., Günther D. and Enzweiler J. (2011) Determination of reference values for NIST SRM 610–617 glasses following ISO guidelines. *Geostand. Geoanal. Res.* **35**, 397–429.

Jugo P. J., Luth R. W. and Richards J. P. (2005) Experimental data on the speciation of sulfur as a function of oxygen fugacity in basaltic melts. *Geochim. Cosmochim. Acta* **69**, 497–503.

Jugo P. J., Wilke M. and Botcharnikov R. E. (2010) Sulfur K-edge XANES analysis of natural and synthetic basaltic glasses. *Geochim. Cosmochim. Acta* **74**, 5926–5938.

Kimura K., Lewis R. S. and Anders E. (1974) Distribution of gold and rhenium between nickel-iron and silicate melts: implications for the abundance of siderophile elements on the Earth and Moon. *Geochim. Cosmochim. Acta* **38**, 683–701.

Kiseeva E. S. and Wood B. J. (2013) A simple model for chalcophile element partitioning between sulphide and silicate liquids with geochemical applications. *Earth Planet. Sci. Lett.* **383**, 68–81.

Kiseeva E. S. and Wood B. J. (2015) The effects of composition and temperature on chalcophile and lithophile element partitioning into magmatic sulphides. *Earth Planet. Sci. Lett.* **424**, 280–294.

Klimm K. and Botcharnikov R. E. (2010) The determination of sulfate and sulfide species in hydrous silicate glasses using Raman spectroscopy. *Am. Mineral.* **95**, 1574–1579.

Kruijer T. S., Kleine T., Fischer-Gödde M. and Sprung P. (2015) Lunar tungsten isotopic evidence for the late veneer. *Nature* **520**, 534–537.

Laurenz V., Fonseca R. O. C., Ballhaus C. and Sylvester P. J. (2010) Solubility of palladium in picritic melts. *Geochim. Cosmochim. Acta* **74**, 2989–2998.

Laurenz V., Fonseca R. O., Ballhaus C., Jochum K. P., Heuser A. and Sylvester P. J. (2013) The solubility of palladium and ruthenium in picritic melts: 2. The effect of sulfur. *Geochim. Cosmochim. Acta* **108**, 172–183.

Lee C.-T. A., Yin Q.-Z., Lenardic A., Agranier A., O'Neill C. J. and Thiagarajan N. (2007) Trace-element composition of Fe-rich residual liquids formed by fractional crystallization: Implications for the Hadean magma ocean. *Geochim. Cosmochim. Acta* **71**, 3601–3615.

Li J. and Agee C. B. (1996) Geochemistry of mantle-core differentiation at high pressure. *Nature* **381**, 686–689.

Li J. and Agee C. (2001) The effect of pressure, temperature, oxygen fugacity and composition on partitioning of nickel and cobalt between liquid Fe–Ni–S alloy and liquid silicate: implications for the earth's core formation. *Geochim. Cosmochim. Acta* **65**, 1821–1832.

Li C. S. and Ripley E. M. (2005) Empirical equations to predict the sulfur content of mafic magmas at sulfide saturation and applications to magmatic sulfide deposits. *Mineral. Deposita* **40**, 218–230.

Li C. S. and Ripley E. M. (2009) Sulfur contents at sulfide-liquid or Anhydrite Saturation in silicate melts: empirical equations and example applications. *Econ. Geol.* **104**, 405–412.

Mann U., Frost D. J. and Rubie D. C. (2009) Evidence for high-pressure core-mantle differentiation from the metal–silicate partitioning of lithophile and weakly-siderophile elements. *Geochim. Cosmochim. Acta* **73**, 7360–7386.

Mann U., Frost D. J., Rubie D. C., Becker H. and Audétat A. (2012) Partitioning of Ru, Rh, Pd, Re, Ir and Pt between liquid metal and silicate at high pressures and high temperatures – implications for the origin of highly siderophile element concentrations in the Earth's mantle. *Geochim. Cosmochim. Acta* **84**, 593–613.

Marty B. (2012) The origins and concentrations of water, carbon, nitrogen and noble gases on Earth. *Earth Planet. Sci. Lett.* **313–314**, 56–66.

Mavrogenes J. A. and O'Neill H. S. C. (1999) The relative effects of pressure, temperature and oxygen fugacity on the solubility of sulfide in mafic magmas. *Geochim. Cosmochim. Acta* **63**, 1173–1180.

McDonough W. F. and Sun S. S. (1995) The composition of the Earth. *Chem. Geol.* **120**, 223–253.

Médard E., Schmidt M. W., Wälle M., Keller N. S. and Günther D. (2015) Platinum partitioning between metal and silicate melts: Core formation, late veneer and the nanonuggets issue. *Geochim. Cosmochim. Acta* **162**, 183–201.

Meisel T., Walker R. J., Irving A. J. and Lorand J. P. (2001) Osmium isotopic compositions of mantle xenoliths. *Geochim. Cosmochim. Acta* **65**, 1311–1323.

Métrich N., Berry A. J., O'Neill, Hugh St. C. and Susini J. (2009) The oxidation state of sulfur in synthetic and natural glasses determined by X-ray absorption spectroscopy. *Geochim. Cosmochim. Acta* **73**, 2382–2399.

Morgan J. W., Walker R. J., Brandon A. D. and Horan M. F. (2001) Siderophile elements in the Earth's upper mantle and lunar breccias. *Meteorit. Planet. Sci.* **36**, 1257–1275.

Mukhopadhyay B., Basu S. and Holdaway M. J. (1993) A discussion of Margules-type formulations for multicomponent solutions with a generalized approach. *Geochim. Cosmochim. Acta* **57**, 277–283.

Mungall J. E. and Brenan J. M. (2014) Partitioning of platinum-group elements and Au between sulfide liquid and basalt and the origins of mantle–crust fractionation of the chalcophile elements. *Geochim. Cosmochim. Acta* **125**, 265–289.

Nagamori M., Hatakeyama T. and Kameda M. (1970) Thermodynamics of Fe–S melts between 1100° and 1300 °C. *Trans. Jpn. Inst. Met.* **11**, 190–194.

Namur O., Charlier B., Holtz F., Cartier C. and McCammon C. (2016) Sulfur solubility in reduced mafic silicate melts: implications for the speciation and distribution of sulfur on Mercury. *Geochim. Cosmochim. Acta* **448**, 102–114.

O'Brien D. P., Morbidelli A. and Levison H. F. (2006) Terrestrial planet formation with strong dynamical friction. *Icarus* **184**, 39–58.

O'Brien D. P., Walsh K. J., Morbidelli A., Raymond S. N. and Mandell A. M. (2014) Water delivery and giant impacts in the 'Grand Tack' scenario. *Icarus* **239**, 74–84.

O'Neill H. S. C. (1991) The origin of the Moon and the early history of the Earth – A chemical model Part 2: the Earth. *Geochim. Cosmochim. Acta* **55**, 1159–1172.

O'Neill H. S. C. and Mavrogenes J. A. (2002) The sulfide capacity and the sulfur content at sulfide saturation of silicate melts at 1400 degrees C and 1 bar. *J. Petrol.* **43**, 1049–1087.

O'Neill H. S. C. and Pownceby M. I. (1993) Thermodynamic data from redox reactions at high temperatures. 1. An experimental and theoretical assessment of the electrochemical method using stabilized zirconia electrolytes, with revised values for the Fe–FeO, Co–CoO, Ni–NiO and Cu–Cu₂O oxygen buffers, and new data for the W-WO2 buffer. *Contrib. Mineral. Petrol.* **114**, 296–314.

O'Neill H. S. C. and Wall V. J. (1987) The olivine-orthopyroxene-spinel oxygen geobarometer, the nickel precipitation curve, and the oxygen fugacity of the Earth's upper mantle. *J. Petrol.* **28**, 1169–1191.

O'Neill H. S. C., Dingwell D. B., Borisov A., Spettel B. and Palme H. (1995) Experimental petrochemistry of some highly siderophile elements at high temperatures, and some implications for core formation and the mantle's early history. *Chem. Geol.* **120**, 255–273.

O'Neill H. S. C., Canil D. and Rubie D. C. (1998) Oxide-metal equilibria to 2500 degrees C and 25 GPa: Implications for core formation and the light component in the Earth's core. *J. Geophys. Res.-Sol. Ea.* **103**, 12239–12260.

Palme H. and O'Neill H. (2014) Cosmochemical estimates of mantle composition. In *Treatise on Geochemistry* (eds. H. D. Turekian and K. K. Holland), second ed. Elsevier, Oxford, pp. 1–39.

Peach C. L., Mathez E. A. and Keays R. R. (1990) Sulfide melt–silicate melt distribution coefficients for noble metals and other chalcophile elements as deduced from MORB: implications for partial melting. *Geochim. Cosmochim. Acta* **54**, 3379–3389.

Pruseth K. L. and Palme H. (2004) The solubility of Pt in liquid Fe-sulfides. *Chem. Geol.* **208**, 233–245.

Righter K. (2011) Prediction of metal–silicate partition coefficients for siderophile elements: an update and assessment of PT conditions for metal–silicate equilibrium during accretion of the Earth. *Earth Planet. Sci. Lett.* **304**, 158–167.

Righter K., Humayun M. and Danielson L. (2008) Partitioning of palladium at high pressures and temperatures during core formation. *Nat. Geosci.* **1**, 321–323.

Righter K., Danielson L., Drake M. J. and Domanik K. (2014) 3.12 – partition coefficients at high pressure and temperature. In

Treatise on Geochemistry (eds. H. D. Turekian and K. K. Holland), second ed. Elsevier, Oxford, pp. 449–477.

Rose-Weston L., Brenan J. M., Fei Y., Secco R. A. and Frost D. J. (2009) Effect of pressure, temperature, and oxygen fugacity on the metal–silicate partitioning of Te, Se, and S. *Geochim. Cosmochim. Acta* **73**, 4598–4615.

Rubie D. C. (1999) Characterising the sample environment in multianvil high-pressure experiments. *Phase Transit.* **68**, 431–451.

Rubie D. C., Melosh H. J., Reid J. E., Liebske C. and Righter K. (2003) Mechanisms of metal–silicate equilibration in the terrestrial magma ocean. *Earth Planet. Sci. Lett.* **205**, 239–255.

Rubie D. C., Frost D. J., Mann U., Asahara Y., Nimmo F., Tsuno K., Kegler P., Holzheid A. and Palme H. (2011) Heterogeneous accretion, composition and core–mantle differentiation of the Earth. *Earth Planet. Sci. Lett.* **301**, 31–42.

Rubie D. C., Jacobson S. A., Morbidelli A., O'Brien D. P., Young E. D., Vries J., de Nimmo F., Palme H. and Frost D. J. (2015) Accretion and differentiation of the terrestrial planets with implications for the compositions of early-formed Solar System bodies and accretion of water. *Icarus* **248**, 89–108.

Rubie D. C., Laurenz V., Jacobson S. A., Morbidelli A., Palme H., Vogel A. K. and Frost D. J. (2016) Highly siderophile elements were stripped from Earth's mantle by iron sulfide segregation. *Science.* http://dx.doi.org/10.1126/science.aaf6919.

Savage P. S., Moynier F., Chen H., Shofner G., Siebert J., Badro J. and Puchtel I. S. (2015) Copper isotope evidence for large-scale sulphide fractionation during Earth's differentiation. *Geochem. Perspect. Lett.* **1**, 53–64.

Sylvester P. and Eggins S. M. (1997) Analysis of Re, Au, Pd, Pt and Rh in NIST glass certified reference materials and natural basalt glasses by laser ablation ICP-MS. *Geostand. Geoanal. Res.* **21**, 215–229.

Thibault Y. and Walter M. J. (1995) The influence of pressure and temperature on the metal–silicate partition-coefficients of nickel and cobalt in a model-C1 chondrite and implications for metal-segregation in a deep magma ocean. *Geochim. Cosmochim. Acta* **59**, 991–1002.

Vogel A. K. (2015) *Siderophile element partitioning at high pressures and temperatures: implications for core formation processes* PhD thesis. Universität Bayreuth, USA, p. 226, <https://epub.uni-bayreuth.de/2039/>.

Wade J. and Wood B. J. (2005) Core formation and the oxidation state of the Earth. *Earth Planet. Sci. Lett.* **236**, 78–95.

Wade J., Wood B. J. and Tuff J. (2012) Metal–silicate partitioning of Mo and W at high pressures and temperatures: evidence for late accretion of sulphur to the Earth. *Geochim. Cosmochim. Acta* **85**, 58–74.

Walker D. (2000) Core participation in mantle geochemistry: geochemical Society Ingerson Lecture, GSA Denver, October 1999. *Geochim. Cosmochim. Acta* **64**, 2897–2911.

Walker R. J. (2009) Highly siderophile elements in the Earth, Moon and Mars. *Chem. Erde-Geochem.* **69**, 101–125.

Walker R. J., Bermingham K., Liu J., Puchtel I. S., Touboul M. and Worsham E. A. (2015) In search of late-stage planetary building blocks. *Chem. Geol.* **411**, 125–142.

Walsh K. J., Morbidelli A., Raymond S. N., O'Brien D. P. and Mandell A. M. (2011) A low mass for Mars from Jupiter's early gas-driven migration. *Nature* **475**, 206–209.

Wang Z. and Becker H. (2013) Ratios of S, Se and Te in the silicate Earth require a volatile-rich late veneer. *Nature* **499**, 328.

Wang Z., Laurenz V., Petitgirard S. and Becker H. (2016) Earth's moderately volatile element composition may not be chondritic: evidence from In, Cd and Zn. *Earth Planet. Sci. Lett.* **435**, 136–146.

Wänke H. (1981) Constitution of the terrestrial planes. *Philos. T. R. Soc. A* **303**, 287–302.

Wasson J. T. and Kallemeyn G. W. (1988) Compositions of chondrites. *Philos. Trans. R. Soc. Assoc.* **325**, 535–544.

Wood B. J. and Halliday A. N. (2005) Cooling of the Earth and core formation after the giant impact. *Nature* **437**, 1345–1348.

Wood B. J., Li J. and Shahar A. (2013) Carbon in the core: its influence on the properties of core and mantle. *Rev. Mineral. Geochem.* **75**, 231–250.

Wood B. J., Kiseeva E. S. and Mirolo F. J. (2014) Accretion and core formation: the effects of sulfur on metal–silicate partition coefficients. *Geochim. Cosmochim. Acta* **145**, 248–267.

Wykes J. L., O'Neill, Hugh St. C. and Mavrogenes J. A. (2015) The effect of FeO on the sulfur content at sulfide saturation (SCSS) and the selenium content at selenide saturation of silicate melts. *J. Petrol.* **56**, 1407–1424.

Associate editor: Richard J. Walker